Fast kinetic simulator for relativistic matter

Document status and date:
Published: 01/10/2022

Document Version:
Publisher's PDF, also known as Version of Record (includes final page, issue and volume numbers)

Please check the document version of this publication:

Fast kinetic simulator for relativistic matter

V. E. Ambruş [1,2], L. Bazzanini [3], A. Gabbana [4], D. Simeoni [3,5,6] ✉, S. Succi [7,8] and R. Tripiccione [3]

Relativistic kinetic theory is ubiquitous to several fields of modern physics, finding application at large scales in systems in astrophysical contexts, all of the way down to subnuclear scales and into the realm of quark–gluon plasmas. This motivates the quest for powerful and efficient computational methods that are able to accurately study fluid dynamics in the relativistic regime as well as the transition to beyond hydrodynamics—in principle all of the way down to ballistic regimes. We present a family of relativistic lattice kinetic schemes for the efficient simulation of relativistic flows in both strongly (fluid) and weakly (rarefied gas) interacting regimes. The method can deal with both massless and massive particles, thereby encompassing ultra- and mildly relativistic regimes alike. The computational performance of the method for the simulation of relativistic flows across the aforementioned regimes is discussed in detail, along with prospects of future applications.

Relativistic fluid dynamics deals with the study of the motion of particles traveling close to the speed of light, as is typically the case in plasma physics, astrophysics and cosmology[1]. In recent years, experimental data from high-energy particles colliders such as the Relativistic Heavy Ion Collider (RHIC) and the Large Hadron Collider (LHC) have provided clear-cut evidence that the exotic state of matter known as quark–gluon plasma (QGP) also behaves like a low-viscosity relativistic fluid[2]. Further evidence started to emerge that electron fluids in exotic two-dimensional materials such as graphene are also described by relativistic hydrodynamics[3]. More generally, in light of the anti-de Sitter-conformal field theory duality[4], relativistic hydrodynamics has acquired a very distinct role as a low-energy effective field theory at the cross-road between high-energy physics, gravity and quantum condensed matter[5–7].

The physics of fluids—classical, quantum and relativistic alike—is characterized by the subtle competition between mechanisms that promote equilibrium (collisions) and mechanisms that sustain the opposite tendency (transport): in Boltzmann's momentous words, "the ever-shifting battle" between equilibrium and non-equilibrium[8].

In relativistic fluids, the above competition is controlled by two dimensionless groups: the relativistic coldness $\zeta = mc^2/k_B T$, which is ratio of the particle's rest energy to its thermal energy; and the Knudsen number, $\mathrm{Kn} = \lambda/\ell$. Here m is the mass of the particle, c the speed of light, T the temperature, k_B is the Boltzmann constant, λ the mean free path and ℓ is a characteristic macro scale.

The relativistic coldness scales like the inverse temperature, hence it takes large values in the non-relativistic regime, in which kinetic energy is small compared with the rest energy. It also scales linearly with the particle mass, which means that high values of coldness correspond with heavy particles, pointing again to the non-relativistic regime. Importantly, the relativistic coldness is an equilibrium property.

The Knudsen number, on the other hand, measures the departure from (local) equilibrium due to the spatial inhomogeneities that drive transport phenomena and dissipation. As the mean free path scales like the inverse density, so does the Knudsen number, which takes up substantial values in the rarefied gas regime, where the hydrodynamic description no longer holds.

In broad strokes the $(\zeta - \mathrm{Kn})$ plane can be split into four quadrants:
1. Relativistic fluids ($\zeta < 1$, $\mathrm{Kn} < 0.01$);

[1]Institut für Theoretische Physik, Johann Wolfgang Goethe-Universität, Frankfurt, Germany. [2]Department of Physics, West University of Timişoara, Timisoara, Romania. [3]Università di Ferrara and INFN-Ferrara, Ferrara, Italy. [4]Eindhoven University of Technology, Eindhoven, Netherlands. [5]Bergische Universität Wuppertal, Wuppertal, Germany. [6]University of Cyprus, Physics department, Nicosia, Cyprus. [7]Center for Life, Nano & Neuro Science @ La Sapienza, Italian Institute of Technology, Roma, Italy. [8]Department of Physics, Harvard University, Cambridge, MA, USA. ✉e-mail: dan.simeoni@gmail.com
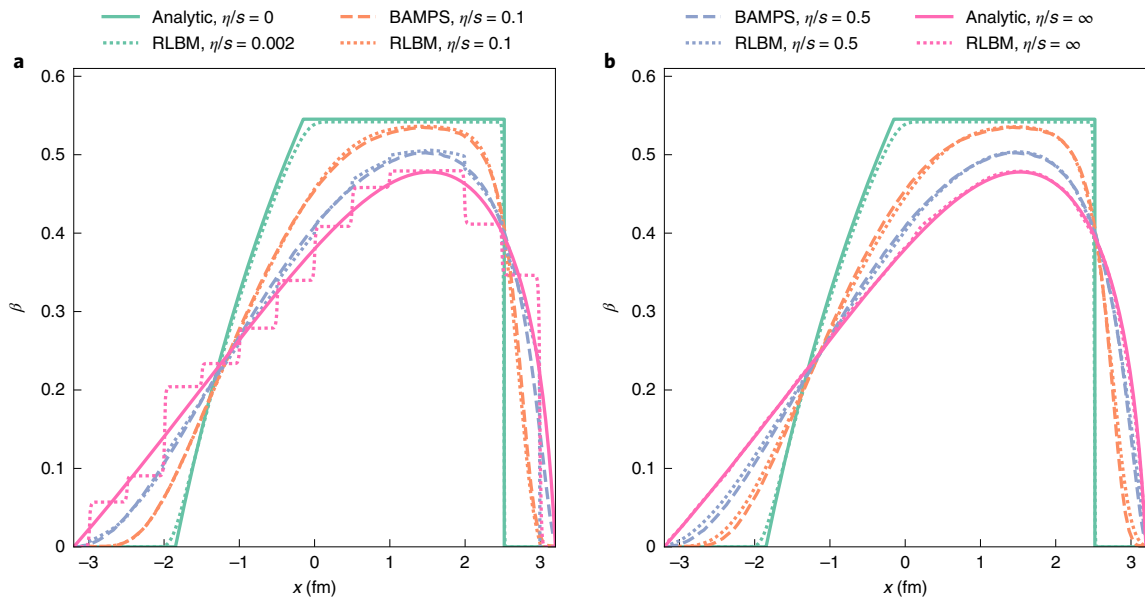
Fig. 1 | Riemann problem for an ultra-relativistic gas of particles for various viscous regimes. We show the macroscopic velocity profile $\beta = U^x/U^0$ at $t = 3.2$ fm/c (1 fm/$c \approx 3.3 \times 10^{-24}$ s), comparing the results of the RLBM against analytical solutions and BAMPS results. **a**, RLBM developed for the hydrodynamic regime[36]. **b**, The high-order RLBM scheme described in this work.

2. Non-relativistic fluids ($\zeta > 1$, Kn < 0.01);
3. Relativistic gases ($\zeta < 1$, Kn > 0.01);
4. Non-relativistic gases ($\zeta > 1$, Kn > 0.01);

The four quadrants above encompass a broad class of vastly different states of matter from (1) QGP to (2) Bose–Einstein condensates, and (3) relativistic and (4) classical astrophysical systems.

Clearly no single numerical method can work seamlessly across such a broad variety of systems; there is a typical separation between fluid-dynamic methods based on the discretization of the fluid equations[9–17] and kinetic methods (mostly Monte Carlo) for the Boltzmann equation[18–23].

Although lattice kinetic methods such as the lattice Boltzmann method[24] offer a potential bridge between these two main families, so far they have been confined to the relativistic fluid sector[25–27] and successfully applied to a number of relativistic hydrodynamic problems in QGP[28,29], electron transport in graphene[30] and also cosmic neutrino transport[31]. A similar approach has been directed to the study of ultra-relativistic gases in (3 + 1)[32] as well as (2 + 1)-dimensions[33,34].

In this paper we extend the lattice kinetic approach to higher-order discrete velocity sets that allow one to handle finite values of the Knudsen number. This approach applies to both massive and massless particles, thereby extending the range of applicability of the method along both directions in the (ζ − Kn) parameter plane. As a result, the method in this work is expected to offer a useful complement to current QGP codes in assisting the experimental activity of the existing collaborations at the RHIC and LHC.

Results

Model overview

In this work we introduce an extension to a numerical method—the relativistic lattice Boltzmann method (RLBM), originally designed for the study of relativistic fluids—that is capable of accurately solving the relativistic Boltzmann equation in the relaxation-time approximation (RTA) for a broad set of kinematic regimes.

The key insight into the development of lattice Boltzmann methods is the realization that the Boltzmann transport equation (in this case expressed in the language of special relativity) can be appropriately truncated and discretized to recover the dynamics at the hydro level. This operation leads to an evolution equation for the probability density function of particle position and momentum, whose moments deliver the sought-after expressions for the hydrodynamic fields. In particular, the key ingredient to the simulation of weakly interacting regimes is represented by a controlled discretization of the momentum space, which is based on the product of two high-order quadrature rules that discretize the various components of momentum: a Gauss–Laguerre rule of order $N + 1$ is employed for the energy component, whereas quadrature rules of order K for the integration of functions on the sphere[35] are considered for the remaining momentum components. The orders $N + 1$ and K of the quadratures employed lead to a number of N_{pop} discrete momenta. We refer the reader to the Methods for the complete details on the definition of the algorithm, whereas in the following we focus on a few examples of applications and benchmarks that highlight the enhanced accuracy of the current scheme in rarefied conditions.

Shock waves in QGP

We start by considering the relativistic Riemann problem—a commonly adopted numerical benchmark in which a tube filled with gas is, initially, at two different states on each side of a membrane placed at $x = 0$—characterized by the particle number density n, temperature T and four-velocity along the x-axis U^x:

$$(n, T, U^x) = \begin{cases} (n_L, T_L, 0) & x < 0 \\ (n_R, T_R, 0) & x > 0 \end{cases}, \quad (1)$$

where the subscripts L and R represent initial conditions on each side of the membrane. Once the membrane is removed, the system develops one-dimensional shock/rarefaction waves that travel along the x-axis. We use the following initial conditions[36]

$$\begin{cases} n_L = 13.575 \, \text{fm}^{-3}, & T_L = 400 \, \text{MeV} \\ n_R = 1.65 \, \text{fm}^{-3}, & T_R = 200 \, \text{MeV} \end{cases}. \quad (2)$$
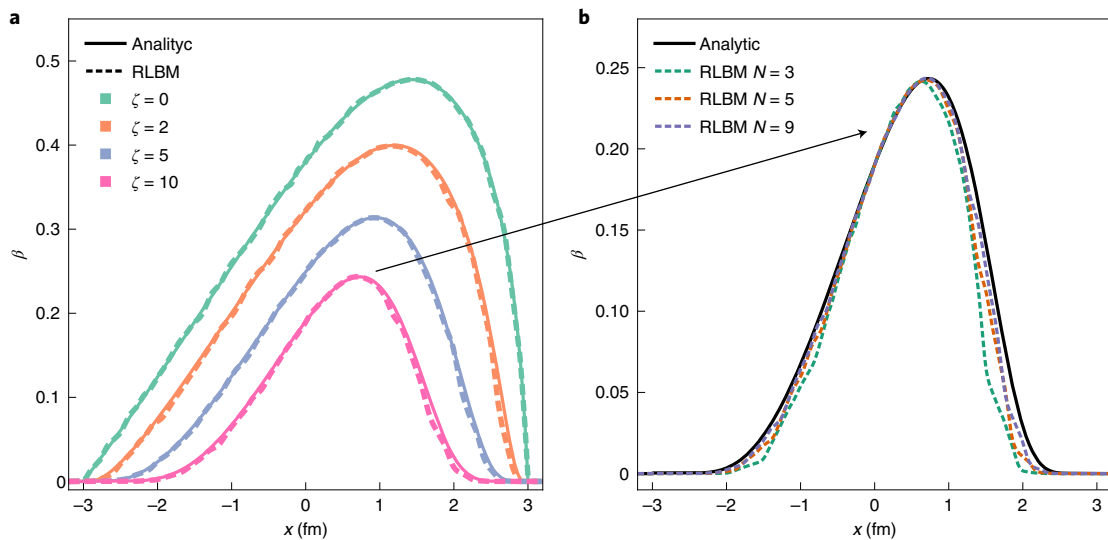
Fig. 2 | Riemann problem for a relativistic gas of particles in the free-streaming regime at different values of *m* corresponding to ζ. Relativistic shock waves for a relativistic gas of particles in the free-streaming. We show the macroscopic velocity profile $\beta = U^x/U^0$ at $t = 3$ fm/c, comparing the results of the RLBM against analytic solutions. The values of $m = (0, 0.8, 2, 4)$ GeV correspond to $\zeta = (0, 2, 5, 10)$. **a**, Results using quadrature rules with $N = 3$, $K = 19$ for $\zeta = (0, 2)$, and $N = 9$, $K = 19$ for $\zeta = (5, 10)$. **b**, Effect of increasing the radial quadrature for $\zeta = 10$.

In simulations we keep the ratio between the shear viscosity (η) and the entropy density (s) fixed to a constant value. For η we use the analytic expressions that result from a first-order Chapman–Enskog expansion[37], whereas the entropy density is given by

$$s = n\left(\zeta\frac{K_3(\zeta)}{K_2(\zeta)} - \ln\left(\frac{n}{n^{\mathrm{eq}}}\right)\right), \qquad (3)$$

with n^{eq} representing the equilibrium density at vanishing chemical potential,

$$n^{\mathrm{eq}} = g\frac{T^3}{2\pi^2}\zeta^2 K_2(\zeta); \qquad (4)$$

where $g = 16$ is the degeneracy factor of gluons and $K_i(\zeta)$ the modified Bessel function of second kind of order i.

For reference, in Fig. 1a we reproduced the results presented in Fig. 1 in the work by Gabbana et al.[36] showing the profile of the macroscopic velocity $\beta = U^x/U^0$ for a gas of massless particles in different kinematic regimes. The two limiting cases—corresponding to the inviscid ($\eta/s \to 0$) and ballistic ($\eta/s \to \infty$) regimes—admit analytical solutions, whereas, for intermediate regimes, we compare the results against a Boltzmann approach to multi-parton scatterings (BAMPS)[19], which solves the Boltzmann equation using Monte Carlo. The on-lattice RLBM model reproduces the solution both in the inviscid and hydrodynamic regimes ($\eta/s = 0.1$). On the other hand, for larger values of η/s, as we move beyond the hydrodynamic regime the macroscopic velocity develops artifacts that become most apparent in the ballistic limit. In Fig. 1b we show that it is possible to improve the accuracy even in rarefied conditions by employing high-order off-lattice quadratures[32]. Here we have used a radial quadrature of order $N = 3$ and an angular quadrature of order $K = 15$ with $N_{\mathrm{pop}} = 480$ discrete components (see Methods for details). We remark that the off-lattice model preserves the same level of accuracy of the on-lattice scheme also in the hydrodynamic regimes.

We now turn to the analysis of a relativistic gas of massive particles; we consider once again the initial conditions given in equation (2), with $m = (0, 0.8, 2, 4)$ GeV. In simulations we normalize quantities with

respect to T_{L} and n_{L} (see equation (1)); the above values thus correspond to $\zeta = (0, 2, 5, 10)$.

In Fig. 2a we compare the results obtained in the free-streaming regime (corresponding to $\eta/s \to \infty$) against analytical solutions, again finding a satisfactory match between the two.

One important remark is that, as the rest mass m of the gas increases, we need to employ a higher-order radial quadrature to match the same level of accuracy achieved in the massless case. This is shown in Fig. 2b, in which we compare the results at $\zeta = 10$, obtained by fixing the angular quadrature at $K = 19$ and increasing the radial quadrature from $N = 3$ (which is the value used for the massless case) up to $N = 9$. The results show the improvements achieved by increasing the degree of accuracy of the radial quadrature.

We now further investigate how the accuracy of the method depends on the degree of K and N by studying the Riemann problem at different Knudsen numbers and relativistic coldnesses.

We use the same initial conditions given by equation (2). To assess the rarefied regime, we make use of the numerical Knudsen number, defined as follows:

$$\mathrm{Kn} = \frac{\tau\langle v \rangle}{L}, \qquad (5)$$

where L defines the spatial resolution chosen for the grid, τ is the relaxation time and $\langle v \rangle$ is a relative mean velocity (taken as c for simplicity). We consider a grid of $L = 1{,}600$ points representing a physical domain of 6.4 fm. As a reference, we take the results of high-resolution RLBM simulations in terms of both grid and momentum discretization, namely, $L = 6{,}400$, $N = 9$ and $K = 31$.

We define the L2 relative error with respect to the temperature field as

$$\epsilon = \frac{||T - T_{\mathrm{hr}}||_2}{||T_{\mathrm{hr}}||_2}, \qquad (6)$$

where hr refers to high-resolution simulations.

In Fig. 3a we plot this observable versus K. All simulations run at a fixed order of the radial quadrature ($N = 3$) and different values of relativistic coldness ($\zeta = 0$ and $\zeta = 5$).
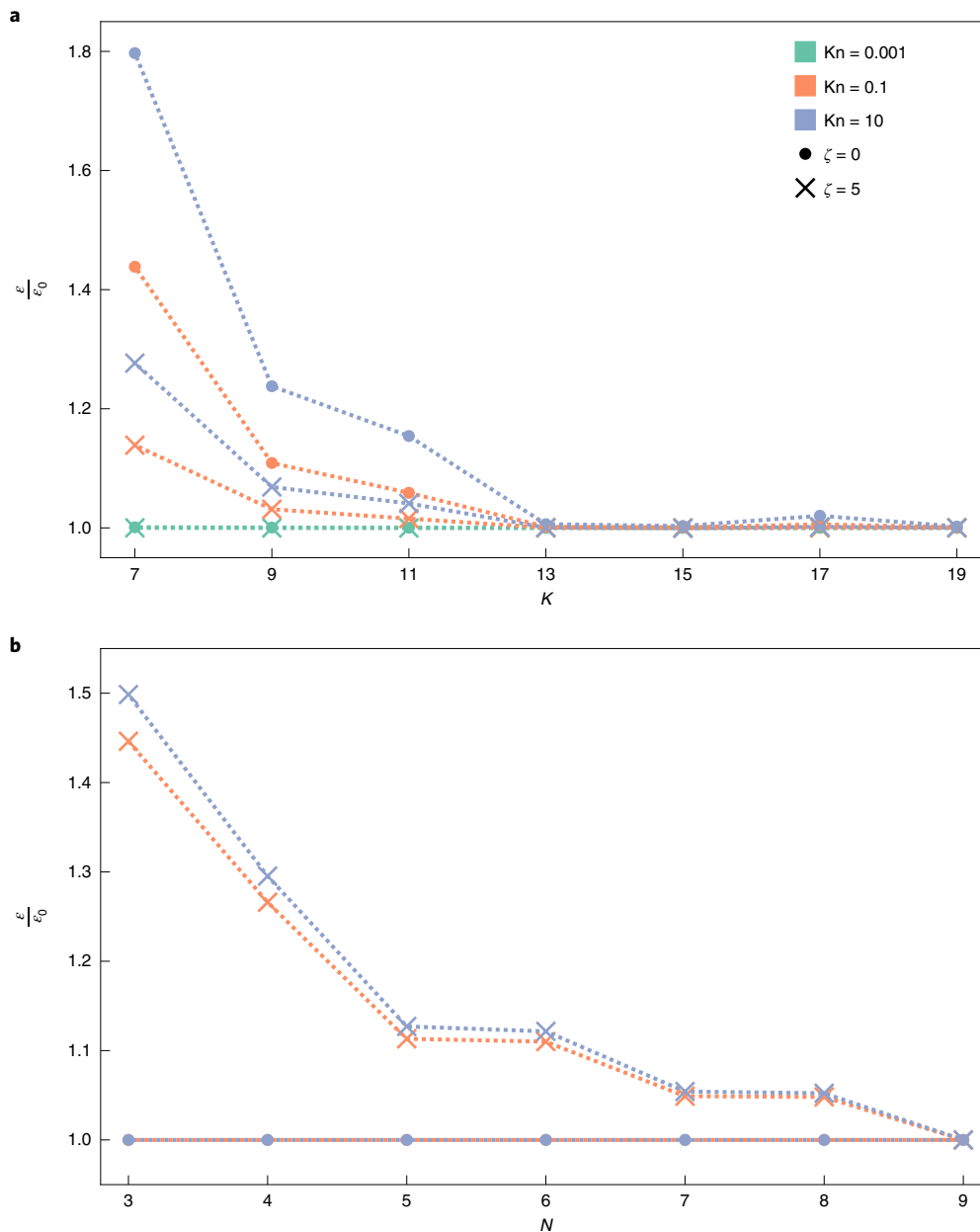
Fig. 3 | Discretization error versus the radial/angular quadrature at different Kn and for different values of the relativistic coldness. The relative error ϵ (equation (6)) is normalized with respect to its asymptotic value ϵ_0. **a**, The effect of increasing the degree of the angular quadrature while keeping the radial quadrature fixed at $N = 3$. Here $\epsilon_0 = \epsilon(K = 19)$. **b**, The effect of increasing the degree of the radial quadrature while keeping the angular quadrature fixed at $K = 13$. Here $\epsilon_0 = \epsilon(K = 9)$.

We can observe the effect of increasing the order of the angular quadrature K by keeping the radial quadrature fixed at $N = 3$. We notice that, as Kn increases, a higher order leads to substantial gains; this effect is more pronounced in the massless case. We also observe that, in the hydrodynamic regime, the accuracy is not affected by the degree of the quadrature.

In Fig. 3b we consider the effect of varying the degree of N while keeping the angular quadrature fixed at $K = 13$. We observe that in the massless case the error does not depend on the radial quadrature, regardless of the value of Kn. On the other hand, at $\zeta = 5$ it is necessary to increase the radial quadrature up to $N = 9$ before saturating the error.

The intuition behind these results is as follows: as massless particles all travel at the speed of light, their discretized components necessarily lie on the surface of a sphere in momentum space. As a

result, increasing K offers a better approximation of momentum space. On the other hand, massive particles cover a finite range of velocities, thus requiring tuning of both the radial and the angular components (see the Methods for more details).

Bjorken attractor
The results presented in the previous section have been obtained from simulations utilizing a uniform Cartesian grid; however, the method can be extended to curvilinear coordinates as well[32,38], which represent the most natural choice for a variety of relativistic flow problems. In this section we focus on such a case, namely, the Bjorken model[39], which is particularly relevant to QGP experiments. Indeed, the existence of Bjorken attractors[40] and the details of their structure have received considerable attention in recent years because they provide valuable information on

the initial conditions right after the collisions, the onset of fluid-dynamic behavior and the material properties of the QGP state of matter (see the recent review by Soloviev[41]). The evolution of the system at very early times (pre-equilibrium phase) along the attractor allows one to estimate the work performed by the QGP against longitudinal expansion, which leads to the overall cooling of the fireball[42]. Moreover, the entropy production in this pre-equilibrium phase can have an effect on the overall particle yields[43]. Another effect of the pre-equilibrium stage is related to the inhomogeneous cooling of the initial state, which leads to modifications to the eccentricity of the transverse profile and of the subsequent build-up of elliptic flow that is characterized by v_2 (ref. [44]).

Next we focus on the early time dynamics of the fireball induced by the rapid longitudinal expansion, which is well described by Bjorken's approximation of longitudinal boost-invariance. For simplicity, we consider the flow of an ideal gas of massless particles, with an ideal equation of state $\epsilon = 3P$, and at constant η/s.

Neglecting the dynamics in the transverse plane, the velocity profile satisfying boost-invariance along the z-direction is

$$U^\alpha \partial_\alpha = \frac{1}{\tau}(t\partial_t + z\partial_z) = \partial_\tau, \quad (7)$$

where U^α is the macroscopic four-velocity and $\tau = \sqrt{t^2 - z^2}$ is the Bjorken time. We employ Bjorken coordinates (τ, x, y, η_s), where $\eta_s = \mathrm{atanh}(z/t)$ is the space−time rapidity (we use the subscript s to distinguish this from the shear viscosity η) and introduce the following observable:

$$\chi = \frac{P_L}{P_T} = \frac{P + \pi_d}{P - \frac{1}{2}\pi_d}, \quad (8)$$

which represents the ratio between the longitudinal and transverse pressures, with $\pi_d = \frac{2}{3}(P_L - P_T)$ being a component of the (dissipative) shear-stress tensor, not to be confused with $\pi \simeq 3.14$ (see Methods for details). The initial state is prepared at vanishing chemical potential, such that $n_0 \equiv n(\tau_0) = gT_0^3/\pi^2$. Moreover, we enforce a constant ratio between the shear viscosity and the entropy density, which in turn fixes the relaxation time to

$$\tau_R = \frac{5\eta/s}{T}\left(1 + \frac{3}{4}\ln\frac{\tau^{4/3}P}{\tau_0^{4/3}P_0}\right). \quad (9)$$

To describe the evolution of χ, it is convenient to employ the scaling variable $\bar{w}$ defined via the following parametrization[45−47]

$$\bar{w} = \frac{5\tau}{4\pi\tau_R}. \quad (10)$$

In Fig. 4 we present numerical results for the evolution of χ corresponding to two sets of 4×4 simulations: one set of results for RLBM and another for hydro. The BAMPS results taken from the work by Ambruş et al.[48] are also shown for a subset of curves. The initial time and temperature are set to $\tau_0 = 0.2$ fm/c and $T_0 = 0.5$ GeV, respectively; η/s takes the values 5, 1, 0.2 and 0.05, which leads to four different values of $\bar{w}_0$. For each value of η/s, four initial values of χ_0 are considered: 1, 0.75, 0.5 and 0.25.

The RTA and hydro attractor curves are shown in Fig. 4. The analytical approximation for the RTA attractor[49] almost completely overlaps with our numerical solution. The approach to the attractor can be clearly seen for both RLBM and hydro, and, most notably, these attractors differ when $\bar{w} \lesssim 1$. In particular, it can be seen that the attractor solution for hydro gives $\chi < 0$, which corresponds to a non-physical negative longitudinal pressure at small $\bar{w}$. The agreement between hydro and RTA is restored when $\bar{w} \gtrsim 1$, both at the level of the attractor solutions and of

the dynamics of the approach to the attractor. BAMPS results are in agreement with the RLBM solution throughout the entire flow regime.

Anisotropic vortical flow

Recent measurements made by the RHIC Solenoidal Tracker at the level of the decay products of the Λ hyperons revealed that the QGP formed during heavy-ion collisions acquires a global polarization[50,51]. Possible mechanisms leading to the polarization of the QGP constituents are the quantum chiral magnetic and chiral vortical effects[52,53] (see also the work by Ambruş and Chernodub[54] for an interplay between chiral and helical[55] vortical effects). Taken together, these effects can explain the global polarization of the Λ hyperons by means of a non-vanishing magnetic field or vorticity on the freeze-out hypersurface. Although the relevance of the chiral magnetic effect strongly depends on the lifetime of the magnetic field in the QGP fireball, vorticity is expected to be long-lived, decaying only due to dissipation caused by shear. Studies have estimated the vorticity to have a sizeable magnitude at freeze-out[56]. The polarization induced by vorticity can be estimated using the Wigner function formalism[57]. Modeling the dynamics of vorticity using hydrodynamics gives a match with the experimental data for the global polarization[58] (that is, along the total angular momentum vector $\mathbf{J}_{sys}$).

In this section we show an example application of our scheme, which aims to simulate the dynamics of an initial vortex configuration in the more simplistic set-up that ignores the longitudinal expansion (this was addressed in the frame of the Bjorken model in the 'Bjorken attractor' section above).

We consider an ultra-relativistic gas in a cubic grid of side 20 fm, with open boundary conditions. Following past works[59,60], we initialize the density and temperature fields with an asymmetric Gaussian shape:

$$T = T_b + T_0 g(x, y, z),$$
$$n = n_b + n_0 g(x, y, z), \quad (11)$$
$$g(x, y, z) = \exp\left(-\frac{x^2}{2\sigma_x^2} - \frac{y^2}{2\sigma_y^2} - \frac{z^2}{2\sigma_z^2}\right).$$

Here $T_b = 80$ MeV and $n_b = 10^{-3}$ fm^{-3} are background values for temperature and density, respectively, whereas $T_0 = 200$ MeV and $n_0 = 4 \times 10^{-3}$ fm^{-3}. We choose the width of the Gaussian bell, along the x, y, z direction as $\sigma_x = 1$ fm, $\sigma_y = 2.6$ fm and $\sigma_z = 2$ fm, respectively. The initial velocity field is chosen as follows:

$$U_x/U_0 = -\frac{y}{\sqrt{x^2+y^2}}\tanh\left(\frac{\sqrt{x^2+y^2}}{r_0}\right),$$
$$U_y/U_0 = \frac{x}{\sqrt{x^2+y^2}}\tanh\left(\frac{\sqrt{x^2+y^2}}{r_0}\right), \quad (12)$$
$$U_z/U_0 = 0$$

where $r_0 = 6$ fm. We apply a cut-off radius of $R = 3$ fm in the $z = 0$ plane, outside of which the velocity field is set to zero.

The central ellipsoid represents the QGP formed in the collision between heavy nuclei. The highly compressed bulk of the system rotates and expands−cooling down in the process. At a later stage, the fireball further expands and cools down so that the system exits the hydrodynamic regime and enters a weakly interacting rarefied regime known as freeze-out.

The freeze-out regime is classified in terms of η/s, which, in QGP, is found to reach the theoretical lower bound of $1/4\pi$ (ref. [61]). To characterize this effect, we have parametrized η/s as a function of the local temperature by using the following expression[62,63]:

$$\eta/s = \begin{cases} 0.681 - 0.0594\left(\frac{T}{T_R}\right) - 0.544\left(\frac{T}{T_R}\right)^2 & T < T_R \\ \frac{1}{4\pi} & T \geq T_R \end{cases} \quad (13)$$
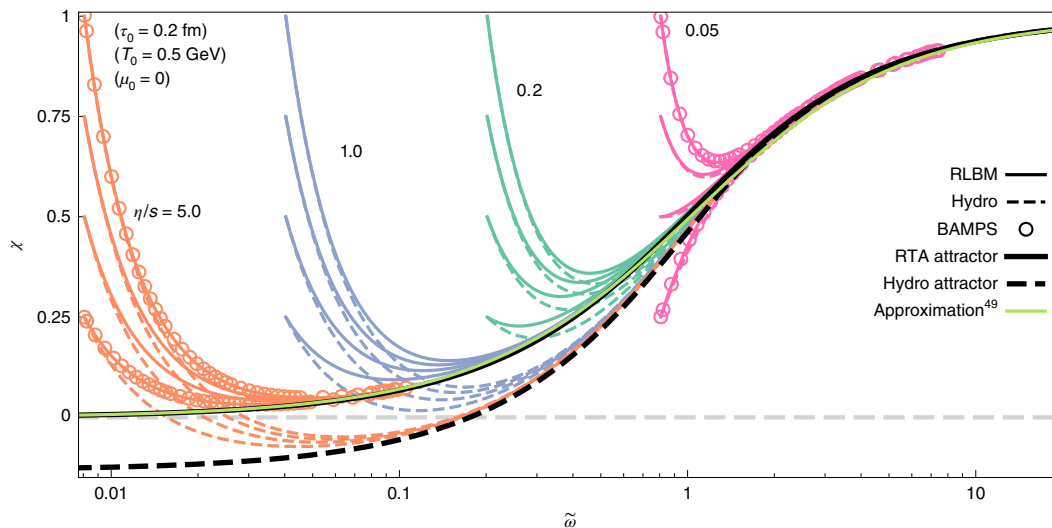
Fig. 4 | Evolution of the pressure anisotropy χ with respect to the scaling variable at initial conditions $\tau_0 = 0.2$ fm/c and $T_0 = 0.5$ GeV, and various values of η/s. Bjorken flow attractor for pressure anisotropy $\chi = P_L/P_T$; $\tilde{\omega}$ is defined in equation (^{10}).

where $T_R = 175$ MeV. In Fig. 5a we show the results of the simulation at $t = 4$fm/c, which were obtained using a high-order off-lattice scheme ($N = 3$, $K = 15$) (Fig. 5b) and an on-grid scheme (Fig. 5c).

Figure 5c shows that the interaction between QGP and the rarefied background gives origin to artifacts (scars in the $(x/\ell, y/\ell) \approx (\pm 0.5, 0)$ region and a general irregularity in the contour lines) not observed in the model in this work.

The comparison shows that the high-order method allows one to cure the artifacts clearly visible in Fig. 5c, in particular at the boundaries of the fireball where the fluid starts to interact with the rarefied region.

Performance data

In this section we give a short overview of the performances of the numerical model. The algorithm in this work has been implemented for the benchmark described in the anisotropic vortical flow section on a single V100-GPU machine using double-precision arithmetics and standard practice optimizations[64,65], delivering about 60 million lattice updates per second (MLUPS) on a 128^3 cubic grid with $N_{pop} = 128$ discrete velocities. This means that the state of the system is advanced over 30 time-steps in a second wall-clock GPU time. For a computational box 10 fm in side, this corresponds to a lattice spacing of about 0.1 fm and a time-step of about 0.1 fm/c. The performance of our code is comparable with that of the GPU implementation of an ideal hydro code[14] while giving access to off-equilibrium dynamics such as dissipation.

Notably, as shown in Fig. 6, the performance scales linearly with the inverse number of components used in the discretization of the momentum space $1/N_{pop}$, falling to about 20 MLUPS for $N_{pop} = 480$. This is an important result as it shows that the code suffers no extra performance penalty in going from the hydro to the quasi-ballistic regime.

As a result, a simulation spanning one million time-steps (10^5 fm/c) completes in roughly 3×10^4 s, that is, about half of a day. As already observed, our method seamlessly describes both hydrodynamic and quasi-ballistic regimes, it can efficiently simulate the long-term evolution of laboratory QGP well into the freeze-out regime and possibly beyond.

Indeed, with suitable coupling to Monte Carlo schemes, by sampling particle positions and momenta from the RLBM solution[66], it may also be possible to describe the rehadronization stage, in which quarks bind back into hadrons[20,22,67–69]. Our scheme can be expected to be between one and two orders of magnitude faster than Monte

Carlo-based implementations such as BAMPS[19,23,48,70], which suffer from statistical noise.

From a mid-term perspective, one may realistically project the current data to large-scale massive parallel GPU architectures such as the Nvidia A100 series. For instance, recent work on multiphase non-relativistic fluids shows that classical lattice Boltzmann schemes with 27 discrete populations can attain up to 100 GLUPS on grids with several billion grid points, using large clusters with hundreds Nvidia A100 GPUs[71,72].

Based on the linear dependence of the GPU performance on the inverse number of populations, one can estimate about 20/5 GLUPS for the case of 100/400 discrete velocities. The same ballpark estimate is obtained by upscaling the current 60 MLUPS to 6 GLUPS on a hundred-GPUs cluster. This means several updates per second for grids with one billion grid points, hence enabling the direct simulation of QGP over three decades in space and twice as many in time, within a few days wall-clock time.

Discussion

In this work we have introduced a lattice kinetic scheme that extends the range of applicability of RLBM to a wider range of kinetic parameters, allowing for the simulation of relativistic gases of massive particles in rarefied conditions.

This paves the way to the systematic study of heavy-ion collisions observables such as the p_T dependence of the flow harmonics $v_n(p_T)$[73] or hadron polarization[58] within kinetic theory. Extending the current scheme to non-ideal fluids can be performed along already discussed lines[29], allowing phenomena related to the quantum chromodynamics phase transition to be explored through large-scale simulations[74–76].

Although a fair comparison between RLBM and Monte Carlo approaches is somehow ill-posed because the latter can handle non-equilibrium effects in full, for systems in which the RTA applies, RLBM can be expected to offer speed increases of one or two orders of magnitude over Monte Carlo methods.

We now point out two limitations of the lattice Boltzmann approach, which are related to the extreme cases of the perfect fluid and of the free-streaming regime. Due to its kinetic nature, our approach can model the ideal fluid only asymptotically by decreasing the relaxation time τ. The limit $\tau \to 0$ becomes expensive in our implementation, which treats the collision term explicitly and therefore the time-step is restricted to satisfy $\delta t < \tau$. For flows in which viscous effects are
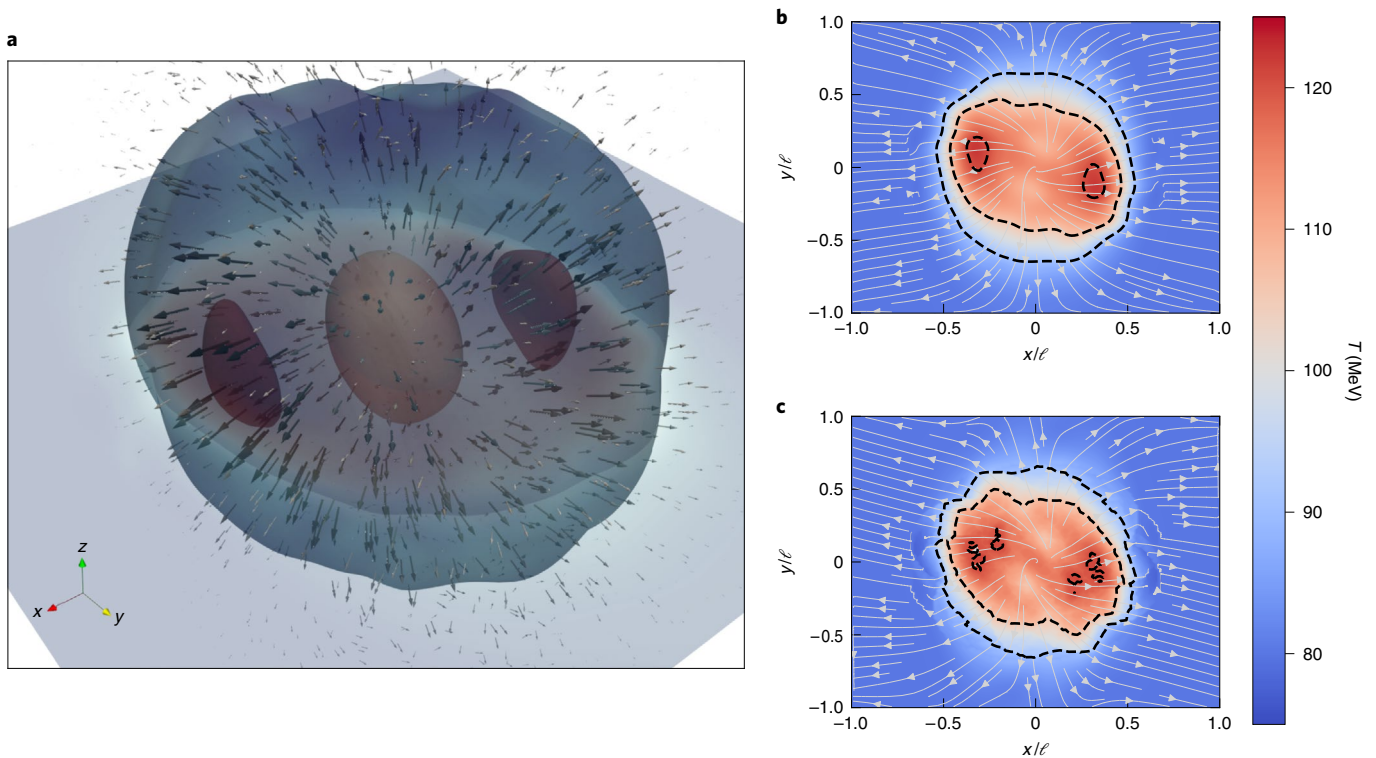
Fig. 5 | Simulation of a vortical flow using set initial conditions and a cubic domain of side ℓ = 20 fm. a, Three-dimensional visualization of the temperature field at $t = 4$ fm/c. Arrows represent the velocity vectors. **b**, Two-dimensional representation of the temperature field at $t = 4$ fm/c for the $z = 0$ plane, using a high-order RLBM. Gray colored lines represent the velocity streamlines, whereas the black dashed lines represent iso-contours of the temperature field. **c**, Same as **b**, but using a RLBM scheme restricted to the simulation of hydrodynamic regimes. The vortical flow is simulated using the initial conditions described in equations (11) and (12).

negligible, directly solving the equations of ideal hydrodynamics as discussed by, for example, Gerhard et al.[14] may be more computationally efficient.

To model the free-streaming limit, the number N_{pop} of discrete distributions must be increased, as can be seen in Fig. 3. As the runtime increases with N_{pop} (see Fig. 6), it is conceivable that flows that are predominantly in this regime may be more efficiently modeled using particle-based approaches such as BAMPS[19].

The present results lay the ground to the computationally efficient large-scale simulations of beyond-hydrodynamic regimes in the framework of QGP experiments. They may also find profitable use in the study of quasi-ballistic electron flows in graphene and possibly also for relativistic flows of astrophysical interest. Furthermore, the implementation of the Boltzmann–Vlasov equation for resistive relativistic magnetohydrodynamics[77,78] is straightforward via the addition of the electromagnetic forcing term, and this in turn might unlock applications in the realm of plasma wakefield acceleration[79].

Methods

In this section we provide full details on the definition of the RLBM, with particular emphasis posed on the momentum space discretization, which is crucial to support the simulation of dynamics at large values of Kn. We start by introducing the notation, with a brief introduction to the main elements of relativistic kinetic theory.

Relativistic kinetic theory

We consider a gas of particles with mass m in a (3 + 1) Minkowski space-time, with metric $\eta^{\alpha\beta} = \text{diag}(+, -, -, -)$. We adopt Einstein's summation convention, with Greek indices running from 0 to 3, and Latin ones from 1 to 3, respectively. We also use natural units: $c = k_B = \hbar = 1$.

Our starting point in the development of the model is the relativistic Boltzmann equation, in the single-relaxation time approximation of Anderson and Witting[80,81]

$$p^\alpha \partial_\alpha f = -\frac{U^\alpha p_\alpha}{\tau}\left(f - f^{eq}\right). \tag{14}$$

This equation describes the evolution of the particle distribution function $f(x^\alpha = (t, \mathbf{x}), p^\alpha = (p^0, \mathbf{p}))$, accounting for the number of particles per unit volume in the six-dimensional single-particle phase space $d^3x\,d^3p$, where $\mathbf{x}$ represents the space coordinate, t represents the time coordinate, $\mathbf{p}$ is the particle momentum vector and p^0 is the particle energy.

U^α is the macroscopic fluid velocity, τ is the (proper)-relaxation time and f^{eq} is the equilibrium distribution function:

$$f^{eq}(p^\alpha, U^\alpha, T) = \frac{(2\pi)^{-3}g}{\exp\left(\frac{p^\alpha U_\alpha - \mu}{T}\right) + a}, \tag{15}$$

where μ is the chemical potential, g is the number of degrees of freedom per constituent, and a is a parameter that selects between the Maxwell–Jüttner ($a = 0$), Fermi–Dirac ($a = 1$) and Bose–Einstein ($a = -1$) distributions. From now on, we will be considering the Maxwell–Jüttner statistics ($a = 0$).

The chemical potential μ can be expressed in terms of the particle number density. For the Maxwell–Jüttner statistics, we have

$$\frac{g}{(2\pi)^3}e^{\mu/T} = \frac{n}{4\pi T^3 \zeta^2 K_2(\zeta)}, \tag{16}$$

where n is the particle number density and K_ν is the modified Bessel function of second kind of index ν.
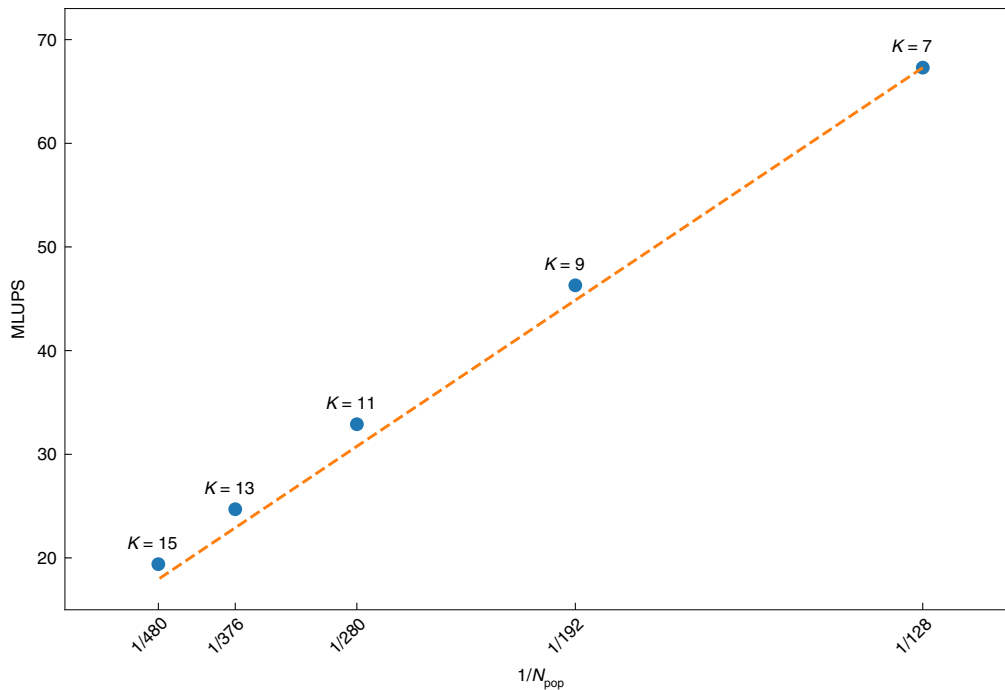
Fig. 6 | Performance scaling with respect to the number of discrete velocities. The results refer to simulations of an ultra-relativistic gas with the following momentum space discretization: $N = 3$, $K =$ variable. The measured performances (blue dots) are expressed in MLUPs. The dashed line represents the linear scaling with respect to $N_{pop} = 128$.

The hydrodynamic fields are related to the lower-order moments of the distribution function, in particular, the first- and second-order moments, namely, the particle flow N^α and energy momentum tensor $T^{\alpha\beta}$,

$$N^\alpha = \int p^\alpha f \frac{\mathrm{d}^3 p}{p^0}, \tag{17}$$

$$T^{\alpha\beta} = \int p^\alpha p^\beta f \frac{\mathrm{d}^3 p}{p^0}. \tag{18}$$

The moments of the distribution can be put in relation to the macroscopic fields via the Landau–Lifschitz[82] decomposition:

$$N^\alpha = nU^\alpha - \frac{n}{P + \epsilon} q^\alpha, \tag{19}$$

$$T^{\alpha\beta} = (P + \epsilon + \varpi)U^\alpha U^\beta - (P + \varpi)\eta^{\alpha\beta} + \pi^{<\alpha\beta>}; \tag{20}$$

where $P(\varpi)$ is the hydrostatic (dynamic) pressure, q^α the heat flux, ϵ the energy density and $\pi^{<\alpha\beta>}$ the pressure deviator. By computing the integrals in equations (17) and (18) at equilibrium, and by matching them with the known expressions of the equilibrium moments N^α_{eq} and $T^{\alpha\beta}_{eq}$, one finds the following ideal equation of state:

$$\epsilon = P\left(\zeta \frac{K_3(\zeta)}{K_2(\zeta)} - 1\right), \quad P = nT, \tag{21}$$

This reduces to the familiar expressions $\epsilon = 3P$ in the ultra-relativistic case ($\zeta \to 0$) and $\epsilon = (3/2)P$ in the non-relativistic case ($\zeta \to \infty$), respectively.

RLBM

We start—after an adimensionalization of variables—by considering an N-truncated expansion of the Maxwell–Jüttner distribution (equation (34)) on a tensorial basis of rank k, $\mathbf{J}^{(k)}(p^\mu)$:

$$f^{eq}(p^\mu, U^\mu, T) = \omega(p^0) \sum_{k=0}^{N} \mathbf{a}^{(k)}(U^\mu, T) \otimes \mathbf{J}^{(k)}(p^\mu), \tag{22}$$

where $\otimes$ represents full tensor contraction. These tensors $\mathbf{J}^{(k)}$ are built as orthogonal polynomials in the variable p^μ with respect to a weighting function $\omega(p^0)$, by using a standard Gram–Schmidt procedure, and can be shown to satisfy the following orthonormality condition:

$$\int \omega(p^0) \mathbf{J}^{(l)}_\alpha(p^\mu) \mathbf{J}^{(k)}_\beta(p^\mu) \frac{\mathrm{d}^3 p}{p^0} = \delta^{lk} \delta_{\alpha\beta}, \tag{23}$$

where $\alpha = \{\alpha_1, ..., \alpha_l\}$ and $\beta = \{\beta_1, ..., \beta_k\}$ are collective tensorial indices introduced for notational conciseness. A detailed discussion and derivation of this set of orthogonal polynomials can be found in the work by Gabbana and colleagues[27]. The expansion coefficients in equation (22) are defined as

$$\mathbf{a}^{(k)}(U^\mu, T) = \int f^{eq}(p^\mu, U^\mu, T)\mathbf{J}^{(k)}(p^\mu)\frac{\mathrm{d}^3 p}{p^0}. \tag{24}$$

The choice of the weight function $\omega(p^0)$ is instrumental: by taking it as the equilibrium distribution in the rest frame, it is possible to establish a direct link between each coefficient $\mathbf{a}^{(k)}$ and the corresponding kth moment of the distribution function.

We next define a quadrature rule satisfying the requirement of preserving all the moments of the distribution up to order N. The quadrature is obtained as product of Gaussian quadratures: we consider a radial quadrature of degree N, which consists of $(N+1)$ discrete components, and an angular quadrature of degree K, which consists of N_K discrete components. This results in a set of $N_{pop} = N_K(N+1)$ discrete momenta $\{p^\mu_i\}$ and corresponding weights $\{w_i\}$, which allows one to define the discretized version of the equilibrium distribution

$$f_i^{\text{eq}} = f^{\text{eq}}(p_i^\mu, U^\mu, T) = w_i \sum_{k=0}^N \mathbf{a}^{(k)}(U^\mu, T) \cdot \mathbf{J}^{(k)}(p_i^\mu). \tag{25}$$

By construction, this recovers all of the moments of the distribution function in the continuum up to order N, and it follows that the integrals in equations (17) and (18) can be computed exactly (that is, equality holds) via discrete sums:

$$N^\alpha = \sum_i^{N_{\text{pop}}} p_i^\alpha f_i, \quad T^{\alpha\beta} = \sum_i^{N_{\text{pop}}} p_i^\alpha p_i^\beta f_i, \tag{26}$$

where $f_i = f_i(\mathbf{x}, t) = f(p_i^\mu, \mathbf{x}, t)$. By combining the quadrature-based discretization of the momentum space with a forward-Euler discretization in time with time-step Δt, it is possible to derive the discrete relativistic lattice Boltzmann equation:

$$f_i(\mathbf{x} + \mathbf{v}_i \Delta t, t + \Delta t) = f_i(\mathbf{x}, t) + \Delta t \frac{p_i^\alpha U_\alpha}{p_i^0 \tau}(f_i^{\text{eq}} - f_i(\mathbf{x}, t)), \tag{27}$$

where $\mathbf{v}_i = \mathbf{p}_i/p_i^0$ is the i-th discretized particle velocity.

We conclude this section with a quick summary of the algorithmic procedure needed to advance equation (27) over a single time step, based on the stream and collide paradigm.

Starting from a suitable initialization $f_i(t = 0)$, at each time step the discrete populations freely stream to the corresponding lattices sites:

$$f_i^*(\mathbf{x}, t) = f_i(\mathbf{x} - \mathbf{v}_i \Delta t, t), \tag{28}$$

This moves information from each lattice point at a distance $\Delta_i \mathbf{x} = \mathbf{v}_i \Delta t$. An interpolation is clearly required whenever $\mathbf{x} - \Delta_i \mathbf{x}$ does not fall on a grid point, to infer the values of the populations at the nodes of the actual Cartesian grid, based on their off-lattice values. In this work we adopt a simple trilinear interpolation scheme:

$$\begin{aligned}
f_i(\boldsymbol{x} - \boldsymbol{v}^i \Delta t, t) = \frac{1}{\Delta x \Delta y \Delta z} \\
\times \{ &f_i(\boldsymbol{x} - \boldsymbol{r}_x - \boldsymbol{r}_y - \boldsymbol{r}_z, t)\left(\Delta t |v_x^i|\right)\left(\Delta t |v_y^i|\right)\left(\Delta t |v_z^i|\right) + \\
&f_i(\boldsymbol{x} - \boldsymbol{r}_y - \boldsymbol{r}_z, t)\left(\Delta x - \Delta t |v_x^i|\right)\left(\Delta t |v_y^i|\right)\left(\Delta t |v_z^i|\right) + \\
&f_i(\boldsymbol{x} - \boldsymbol{r}_x - \boldsymbol{r}_z, t)\left(\Delta t |v_x^i|\right)\left(\Delta y - \Delta t |v_y^i|\right)\left(\Delta t |v_z^i|\right) + \\
&f_i(\boldsymbol{x} - \boldsymbol{r}_x - \boldsymbol{r}_y, t)\left(\Delta t |v_x^i|\right)\left(\Delta t |v_y^i|\right)\left(\Delta z - \Delta t |v_z^i|\right) + \\
&f_i(\boldsymbol{x} - \boldsymbol{r}_x, t)\left(\Delta t |v_x^i|\right)\left(\Delta y - \Delta t |v_y^i|\right)\left(\Delta z - \Delta t |v_z^i|\right) + \\
&f_i(\boldsymbol{x} - \boldsymbol{r}_y, t)\left(\Delta x - \Delta t |v_x^i|\right)\left(\Delta t |v_y^i|\right)\left(\Delta z - \Delta t |v_z^i|\right) + \\
&f_i(\boldsymbol{x} - \boldsymbol{r}_z, t)\left(\Delta x - \Delta t |v_x^i|\right)\left(\Delta y - \Delta t |v_y^i|\right)\left(\Delta t |v_z^i|\right) + \\
&f_i(\boldsymbol{x}, t)\left(\Delta x - \Delta t |v_x^i|\right)\left(\Delta y - \Delta t |v_y^i|\right)\left(\Delta z - \Delta t |v_z^i|\right)\}
\end{aligned} \tag{29}$$

with

$$\begin{cases}
\mathbf{r}_x = \text{sgn}(v_x^i)(\Delta x)\hat{\mathbf{x}} \\
\mathbf{r}_y = \text{sgn}(v_y^i)(\Delta y)\hat{\mathbf{y}} \\
\mathbf{r}_z = \text{sgn}(v_z^i)(\Delta z)\hat{\mathbf{z}},
\end{cases} \tag{30}$$

(v_x^i, v_y^i, v_z^i) being the components of the velocity vectors in the stencil.

Next, the first- and second-order moments N^μ and $T^{\mu\nu}$ are computed using equation (26). The energy density ϵ, U^α and n are obtained by solving the following eigenvalue problem:

$$\begin{aligned}
\epsilon U^\alpha &= T^{\alpha\beta} U_\beta, \\
n &= U^\alpha N_\alpha,
\end{aligned} \tag{31}$$

allowing the thermodynamic quantities μ and T to be recovered from equations (16) and (21).

At this stage, it is possible to compute the local equilibrium distribution (equation (25)), which is needed to apply the collisional operator:

$$f_i(\mathbf{x}, t + \Delta t) = f_i^*(\mathbf{x}, t) + \Delta t \frac{p_i^\alpha U_\alpha}{p_i^0 \tau}(f_i^{\text{eq}} - f_i^*(\mathbf{x}, t)). \tag{32}$$

Momentum space discretization

In this section we present a detailed discussion of the momentum space discretization. We make use of off-lattice quadratures, which are developed as product of Gaussian quadratures[32,34], offering the possibility of handling more complex equilibrium distribution functions and, in turn, extending the applicability of the method to regimes beyond hydrodynamics.

We define a quadrature of order N as a quadrature having the property of preserving exactly (that is, equality holds when integrals are calculated with discrete summations) the first N moments of the particle distribution. Formally, this can be expressed by requiring that all the integrals in the form:

$$I^{\alpha_1 \cdots \alpha_k} = \int \omega(p_0) p^{\alpha_1} \cdots p^{\alpha_k} \frac{\mathrm{d}^3 p}{p_0}, \tag{33}$$

must be exactly computed by the quadrature $\forall k \le 2N$.

As already stated, the weight function $\omega(p^0)$ is proportional to the equilibrium distribution function computed in the rest frame ($U^\alpha = (c, 0, 0, 0)$)

$$\omega(p^0) = C \exp\left(-\frac{p^0}{T}\right), \tag{34}$$

where C is a factor such that $\omega(p^0)$ is normalized to unity.

By introducing the following change of variables

$$\begin{cases}
p^0 = y + m \\
p^x = \sqrt{y(y+2m)} \sin\theta \cos\varphi \\
p^y = \sqrt{y(y+2m)} \sin\theta \sin\varphi \\
p^z = \sqrt{y(y+2m)} \cos\theta
\end{cases}, \tag{35}$$

Equation (33) can be split into two parts

$$I^{\alpha_1 \cdots \alpha_k} = I_R \times I_\Omega, \tag{36}$$

the angular part I_Ω

$$I_\Omega = \int (\sin\theta\cos\varphi)^{k_x}(\sin\theta\sin\varphi)^{k_y}(\cos\theta)^{k_z} \mathrm{d}\Omega, \tag{37}$$

and the radial part I_R

$$I_R = \int_0^{+\infty} W(y) Q(y) \mathrm{d}y, \tag{38}$$

where

$$k = k_0 + k_x + k_y + k_z = k_0 + K \tag{39}$$

$$W(y) = \sqrt{y(y+2m)}\,\omega(y+m) \tag{40}$$

$$Q(y) = (y+m)^{k_0}(y^2 + 2my)^{\frac{K}{2}} \tag{41}$$

and all k_0, k_x, k_y and k_z account for the number of occurrences of the various degrees of freedom in $I^{\alpha_1 \dots \alpha_k}$.

Radial discretization. We focus now on the discretization of the radial integrals. We consider I_R with K as an even number, as, by symmetry, the angular integral I_Ω cancels out for odd values of K.

From equation (41) we observe that in this case $Q(y)$ is a polynomial of degree k, and therefore it is possible to establish a Gauss-like quadrature rule to perform an exact integration of I_R. To this aim we consider the following polynomial basis:

$$P_0 = \mathbf{J}^{(0)}, P_1 = \mathbf{J}^{(1)}_0, \dots, P_{2N} = \mathbf{J}^{(2N)}_{0 \dots 0} \tag{42}$$

that constitutes an orthogonal basis with respect to the weight $W(y)$ defined in equation (40); here the polynomials $\mathbf{J}^{(k)}$ are the ones introduced before in equation (22), and are taken with all indices equal to zero. By referring to the theory of Gaussian quadratures[83], one can derive the Nth order radial quadrature rule in the following way:

$$\text{abscissae } y_i : \quad \text{roots of } P_{N+1}(y), \tag{43}$$

$$\text{weights } w'^{(y)}_i : \quad \int_0^{+\infty} \frac{W(y) P_{N+1}(y)}{(y - y_i) P'_{N+1}(y_i)} \, dy. \tag{44}$$

The corresponding values for the discrete energy, the absolute value of the momentum and velocity can be recovered from the discrete coordinate y_i through equation (35).

For the special case $m = 0$ our procedure coincides with the generalized Gauss–Laguerre quadrature rule.

Angular discretization. Let us now turn to the discretization of the angular part; notice that the angular integral is independent on the mass of the particles. One has

$$I_\Omega = \int (\sin\theta\cos\varphi)^{k_x} (\sin\theta\sin\varphi)^{k_y} (\cos\theta)^{k_z} \, d\Omega. \tag{45}$$

The integrand can be recast into a sum of spherical harmonics $Y_\ell^m(\theta, \varphi)$ of maximum degree K. Therefore any spherical quadrature that integrates exactly all spherical harmonics up to order $\ell = K$ is a proper candidate for our goal. We therefore shift the problem to the exact discrete computation of

$$\int Y_\ell^m(\theta, \varphi) \, d\Omega = \sum_{q=1}^{N_{\text{pop}}} w_q Y_\ell^m(\theta_q, \varphi_q), \quad \forall \ell \le K. \tag{46}$$

Several different spherical quadrature rules are available in the literature (see Weih et al.[31] for a few examples). In this work we adopt spherical design quadratures[84], and in particular we use the sets of stencils already defined in the literature[85].

Decoupling of the radial and angular quadratures. With the procedures described in the previous sections, the nodes and weights of the whole stencil are expressed as

$$\begin{cases} p_{ij}^0 = y_i + m \\ p_{ij}^x = \sqrt{y_i(y_i + 2m)} \sin\theta_j \cos\varphi_j \\ p_{ij}^y = \sqrt{y_i(y_i + 2m)} \sin\theta_j \sin\varphi_j \\ p_{ij}^z = \sqrt{y_i(y_i + 2m)} \cos\theta_j \end{cases}, \tag{47}$$

$$w_{ij} = w'^{(y)}_i w'^{(\theta,\varphi)}_j, \quad \begin{array}{l} i = 1, \dots, N+1 \\ j = 1, \dots, N_K \end{array}. \tag{48}$$

The (minimum) number of discrete components required to implement the quadrature is then $N_{\text{pop}} = N_K(N+1)$. When working in the hydrodynamic regime, one is generally interested in defining the quadrature with the minimal number of discrete components, to minimize the computational cost of the numerical method.

On the other hand, when moving to regimes characterized by high values of Kn, stencils with more than the minimum amount of required discrete velocities are needed because, as the gas becomes more and more rarefied, even small errors in the velocities space become increasingly detrimental to the numerical solution.

One way to achieve better solutions is therefore to increase the number of discrete velocities per energy shell, which, however, comes at an increased computational cost. Another possible action that enhances the solution is the decoupling of the radial and angular abscissae; indeed, once we have accepted to work off-lattice and granted the required isotropy level for recovering the requested moments of the distributions, the restriction of using the same angular stencils for each energy shell p_i^0 can be relaxed. In this way, one can enhance the isotropy of the stencil without having to increase the whole quadrature order.

In $(2+1)$ dimensions this is easily achieved by rotating the sub-stencils related to different energy shells each with a different angle, in such a way that the discrete velocities cover the velocity space in the most homogeneous possible way. Further details can be found in the work by Bazzanini et al.[34] for the $(2+1)$ ultra-relativistic case.

In $(3+1)$ dimensions the decoupling process is not trivial anymore, since we have a relative freedom in the specification of the rotations between the sub-stencils. In fact, having considered an initial velocity set, derived using one of the spherical design quadrature exposed above, then one has, for a radial quadrature of order N, $N+1$ overlapped shells of vectors G_i belonging to the set $G = \bigcup_i^{N+1} G_i$.

Then one has to determine the set of angles $\{\alpha_i, \gamma_i\}$, with $i = 1 \dots N+1$, that defines the rotation matrix

$$R(\alpha_i, \gamma_i) = \begin{pmatrix} \cos\alpha_i \cos\gamma_i & -\sin\alpha_i & \cos\alpha_i \sin\gamma_i \\ \sin\alpha_i \cos\gamma_i & \cos\alpha_i & \sin\alpha_i \sin\gamma_i \\ -\sin\gamma_i & 0 & \cos\gamma_i \end{pmatrix}. \tag{49}$$

The stencil G' is then defined as $G' = \bigcup_i^{N+1} R(\alpha_i, \gamma_i) \cdot G_i$.

There are several approaches with which one can find the different rotation matrices $R(\alpha_i, \gamma_i)$. Here we adopt the following:

- Once a radial discretization order N is set, one obtains $N+1$ energy shells, and consequently $N+1$ velocity subsets G_i, $i = 1, \dots, N+1$.
- Depending on the value of N one adopts the following strategies:

  - When $N+1 = (4, 6, 8, 12, 20)$, we identify Platonic Solids with $N+1$ vertexes. The rotation matrices $R(\alpha_i, \gamma_i)$ are then the ones that map one vertex of the solid to its other vertexes.
  - Instead, for generic values of N, the $R(\alpha_i, \gamma_i)$ matrices are determined by solving the Thomson problem[86], which is related to the minimization of electrostatic energy of electrons constrained on the sphere. Indeed, by treating discrete velocities as electrons, one can determine the $R(\alpha_i, \gamma_i)$ matrices by iteratively joining the sub-stencils G_i and solving the associated Thomson problem for α_i and γ_i.

Bjorken flow in curvilinear coordinates

In this section we provide the algorithmic details required for the solution of the Bjorken flow in curvilinear coordinates presented in the main text.

We consider Bjorken coordinates (τ, x, y, η_s) with Bjorken time $\tau = \sqrt{t^2 - z^2}$, and space–time rapidity $\eta_s = \text{atanh}(z/t)$. We consider a flow

described by boost-invariant velocity profile along the z-direction, neglecting the dynamics in the transverse plane:

$$U^\alpha \partial_\alpha = \frac{1}{\tau}(t\partial_t + z\partial_z) = \partial_\tau. \tag{50}$$

Under these settings the first and second-order moments of the particle distribution function reduce to

$$N^\alpha = (n, 0, 0, 0), \quad T^{\alpha\beta} = \mathrm{diag}(\epsilon, P_\mathrm{T}, P_\mathrm{T}, \tau^{-2}P_\mathrm{L}). \tag{51}$$

where P_T and P_L are the transversal and the longitudinal pressure, respectively. Moreover, the diffusion current vanishes, while the pressure deviator $\pi^{\mu\nu}$ takes a diagonal form, $\pi^{\mu\nu} = \mathrm{diag}(0, -\pi_d/2, -\pi_d/2, \tau^{-2}\pi_d)$, with $\pi_d = \frac{2}{3}(P_\mathrm{L} - P_\mathrm{T})$. The conservation equation $\nabla_\mu N^\mu = 0$ reduces to

$$\tau \frac{\partial(\tau n)}{\partial \tau} = 0, \tag{52a}$$

which has the obvious solution $n = n_0\tau_0/\tau$, with n_0 being the particle number density at initial time τ_0. The conservation equation for the energy momentum tensor, $\nabla_\mu T^{\mu\nu} = 0$, reduces to

$$\tau \frac{\partial\epsilon}{\partial\tau} + \epsilon + P + \pi_d = 0. \tag{52b}$$

The evolution equation for π_d depends on the employed theory. In the frame of the Israel–Stewart second-order hydrodynamics[87,88], it reads[89]

$$\tau \frac{\partial\pi_d}{\partial\tau} + \left(\lambda + \frac{\tau}{\tau_\mathrm{R}}\right)\pi + \frac{16}{15}P = 0, \tag{52c}$$

where $\lambda = 38/21$, and $\tau_\mathrm{R} = 5\eta/4P$ is the Anderson–Witting relaxation time. As P and π_d depend only on τ, equation (52) can be solved easily, for example, by using Runge–Kutta time stepping.

The evolution of π_d can be obtained also from the kinetic equation by writing equation (14) with respect to the Bjorken coordinates, taking into account the degrees of freedom $p = p^\tau$, $v_z = \tau p^\eta/p$ and $\varphi = \arctan(p^y/p^x)$[42]

$$\left(\partial_\tau - \frac{v_z(1-v_z^2)}{\tau}\partial_{v_z} - \frac{v_z^2 p}{\tau}\partial_p\right)f = -\frac{v^\mu u_\mu}{\tau_R}(f - f^\mathrm{eq}), \tag{53}$$

where $v_z = \cos\theta$ in the language of the momentum space discretization section. For simplicity, f^eq is taken as the Maxwell–Jüttner distribution given in equation (34), which reduces in the case of massless particles to

$$f^\mathrm{eq} = \frac{n}{8\pi T^3} \exp\left(-\frac{p^\alpha U_\alpha}{T}\right). \tag{54}$$

The distribution function is initialized using the Romatschke–Strickland distribution [90,91],

$$f_\mathrm{RS} = \frac{g e^{\alpha_0}}{(2\pi)^3} \exp\left[-\frac{1}{\Lambda_0}\sqrt{(p \cdot u)^2 + \xi_0(p \cdot \hat{z})^2}\right], \tag{55}$$

where $\hat{z}^\mu$ is the unit-vector along the rapidity coordinate and $g = 16$ is the number of gluonic degrees of freedom. The parameters α_0, Λ_0 and ξ_0 can be used to set the initial values n_0, P_0 and χ_0, as indicated in equations (11)–(13) by Ambruş and co-workers[48] (see also the work by Strickland and Tantary[45]).

In solving equation (53), it is convenient to take advantage of the azimuthal symmetry of the set-up in both the coordinate and the momentum space, such that f becomes independent of φ. This is equivalent to discretizing the azimuthal direction φ using just one point,

taken as $\varphi = 0$ for definiteness. The v_z and p degrees of freedom can be discretized using the Gauss–Legendre and Gauss–Laguerre quadrature rules of orders K and $N + 1$, respectively[28,32]. By this procedure, the discrete values $v_{z;j}$ ($1 \le j \le K$) and p_k ($1 \le k \le N+1$) are given by the roots of the Legendre and Laguerre polynomials $P_K(v_z)$ and $L_{N+1}^{(2)}(p)$, respectively. As shown in a work by Ambruş and Blaga[32], employing $N = 1$ fully recovers the dynamics of the macroscopic quantities n, P_L and P_T. The corresponding discrete values p_k are $p_1 = 2T_0$ and $p_2 = 6T_0$, where T_0 is taken as the initial temperature[32]. The total number of discrete momentum vectors employed for the simulations presented in this section is thus $2K$. The expansions of f^eq reads

$$f^\mathrm{eq} = \frac{n\, e^{-p/T_0}}{8\pi T_0^3}\left[1 + \left(1 - \frac{T}{T_0}\right)\left(3 - \frac{p}{T_0}\right)\right]. \tag{56}$$

The analogous expression for f_RS was presented by Ambruş and Guga-Roşian[38], however, we do not include it here as it is more complicated due to its explicit dependence on v_z.

Introducing the populations f_{jk} corresponding to the discrete values $(v_{z;j}, p_k)$ of the momentum space degrees of freedom via

$$f_{jk} = 2\pi T_0^3 e^{p_k/T_0} w_j^P w_k^L f(p_k, v_{z;j}, \varphi = 0), \tag{57}$$

where w_j^P and w_k^L are the Gauss–Legendre and Gauss–Laguerre quadrature weights, respectively ($w_1^L = 1.5$ and $w_2^L = 0.5$ when $N = 1$), the quantities n, P_L and P_T are computed via

$$n = \sum_{j=1}^{K}\sum_{k=1}^{N+1} f_{jk},$$

$$P_\mathrm{L} = \sum_{j=1}^{K}\sum_{k=1}^{N+1} p_k v_{z;j}^2 f_{jk}, \tag{58}$$

$$P_\mathrm{T} = \frac{1}{2}\sum_{j=1}^{K}\sum_{k=1}^{N+1} p_k(1 - v_{z;j}^2)f_{jk}.$$

The derivatives of f with respect to v_z and p appearing in equation (53) can be computed via projection onto the Legendre and Laguerre polynomials, respectively leading to linear relations. In the former case, we have

$$\left[\frac{\partial[v_z(1-v_z^2)f]}{\partial v_z}\right]_{jk} = \sum_{j'=1}^{K} \mathcal{K}_{j,j'}^P f_{j',k}, \tag{59}$$

where the kernel matrix $\mathcal{K}_{j,j'}^P$ depending only on K, can be pre-computed. The explicit expression of its elements has been given in equation (3.54) in the work by Ambruş and Blaga[32].

For the derivative with respect to p, we can take advantage that $N = 1$ is fixed and write

$$\left[\frac{1}{p^2}\frac{\partial(fp^3)}{\partial p}\right]_{j,1} = -\left[\frac{1}{p^2}\frac{\partial(fp^3)}{\partial p}\right]_{j,2} = \frac{1}{2}f_{j1} + \frac{3}{2}f_{j2}. \tag{60}$$

Following the discretization of the momentum space, equations (59) and (60) can be employed to replace equation (53) by an ordinary differential equation for the evolution of f_{jk},

$$\partial_\tau f_{jk} = L_{jk}[\tau, f], \tag{61}$$

where $L_{jk}[\tau, f]$ depends on all discrete populations $f_{j',k'}$ evaluated at time τ, as well as on τ. We employ the third-order Runge–Kutta algorithm to evolve the system from time τ to $\tau + \delta\tau$ via two intermediate stages[32],

$$f_{jk}^{(1)}(\tau) = f_{jk}(\tau) + \delta\tau L_{jk}[\tau, f],$$

$$f_{jk}^{(2)}(\tau) = \frac{3}{4}f_{jk}(\tau) + \frac{1}{4}f_{jk}^{(1)}(\tau) + \frac{1}{4}\delta\tau L_{jk}[\tau + \delta\tau, f^{(1)}], \tag{62}$$

$$f_{jk}(\tau + \delta\tau) = \frac{1}{3}f_{jk}(\tau) + \frac{2}{3}f_{jk}^{(2)}(\tau) + \frac{2}{3}\delta\tau L_{jk}[\tau + \delta\tau/2, f^{(2)}].$$

Data availability

Source Data are provided with this paper.

Code availability

The code—as well as examples running the Riemann problem, data and scripts, to reproduce Figs. 1, 2 and 4—has been deposited to Code Ocean[92].

References

1. Rezzolla, L. & Zanotti, O. *Relativistic Hydrodynamics* (Oxford Univ. Press, 2013).
2. Florkowski, W., Heller, M. P. & Spaliński, M. New theories of relativistic hydrodynamics in the LHC era. *Rep. Prog. Phys.* **81**, 046001 (2018).
3. Lucas, A. & Fong, K. C. Hydrodynamics of electrons in graphene. *J. Phy. Condens. Matter* **30**, 053001 (2018).
4. Maldacena, J. The large-N limit of superconformal field theories and supergravity. *Int. J. Theor. Phys.* **38**, 1113–1133 (1999).
5. Romatschke, P. & Romatschke, U. R*elativistic Fluid Dynamics In and Out of Equilibrium: And Applications to Relativistic Nuclear Collisions* (Cambridge Univ. Press, 2019).
6. Lucas, A., Davison, R. A. & Sachdev, S. Hydrodynamic theory of thermoelectric transport and negative magnetoresistance in Weyl semimetals. *Proc. Natl Acad. Sci. USA* **113**, 9463–9468 (2016).
7. Succi, S. Lattice Boltzmann 2038. *Europhys. Lett.* **109**, 50001 (2015).
8. Boltzmann, L. *Lectures on Gas Theory* (Univ. California Press, 2020).
9. Rischke, D. H., Bernard, S. & Maruhn, J. A. Relativistic hydrodynamics for heavy ion collisions. 1. General aspects and expansion into vacuum. *Nucl. Phys. A* **595**, 346–382 (1995).
10. Huovinen, P., Kolb, P. F., Heinz, U., Ruuskanen, P. V. & Voloshin, S. A. Radial and elliptic flow at RHIC: further predictions. *Phys. Lett. B* **503**, 58–64 (2001).
11. Aguiar, C. E., Kodama, T., Osada, T. & Hama, Y. Smoothed particle hydrodynamics for relativistic heavy-ion collisions. *J. Phys. G* **27**, 75–94 (2000).
12. Schenke, B., Jeon, S. & Gale, C. (3+1)D Hydrodynamic simulation of relativistic heavy-ion collisions. *Phys. Rev. C* **82**, 014903 (2010).
13. Molnar, E., Niemi, H. & Rischke, D. H. Numerical tests of causal relativistic dissipative fluid dynamics. *Eur. Phys. J. C* **65**, 615–635 (2010).
14. Gerhard, J., Lindenstruth, V. & Bleicher, M. Relativistic hydrodynamics on graphic cards. *Comput. Phys. Commun.* **184**, 311–319 (2013).
15. Del Zanna, L. et al. Relativistic viscous hydrodynamics for heavy-ion collisions with ECHO-QGP. *Eur. Phys. J. C* **73**, 2524 (2013).
16. Karpenko, I., Huovinen, P. & Bleicher, M. A 3+1 dimensional viscous hydrodynamic code for relativistic heavy ion collisions. *Comput. Phys. Commun.* **185**, 3016–3027 (2014).
17. Pandya, A., Most, E. R. & Pretorius, F. Conservative finite volume scheme for first-order viscous relativistic hydrodynamics. *Phys. Rev. D* **105**, 123001 (2022).
18. Nonaka, C., Honda, E. & Muroya, S. (3+1)-Dimensional relativistic hydrodynamical expansion of hot and dense matter in ultra-relativistic nuclear collision. *Eur. Phys. J. C* **17**, 663–673 (2000).
19. Xu, Z. & Greiner, C. Transport rates and momentum isotropization of gluon matter in ultrarelativistic heavy-ion collisions. *Phys. Rev. C* **76**, 024911 (2007).
20. Petersen, H., Steinheimer, J., Burau, G., Bleicher, M. & Stöcker, H. A fully integrated transport approach to heavy ion reactions with an intermediate hydrodynamic stage. *Phys. Rev. C* **78**, 044901 (2008).
21. Plumari, S., Puglisi, A., Scardina, F. & Greco, V. Shear viscosity of a strongly interacting system: Green–Kubo correlator versus Chapman–Enskog and relaxation-time approximations. *Phys. Rev. C* **86**, 054902 (2012).
22. Weil, J. et al. Particle production and equilibrium properties within a new hadron transport approach for heavy-ion collisions. *Phys. Rev. C* **94**, 054905 (2016).
23. Gallmeister, K., Niemi, H., Greiner, C. & Rischke, D. H. Exploring the applicability of dissipative fluid dynamics to small systems by comparison to the Boltzmann equation. *Phys. Rev. C* **98**, 024912 (2018).
24. Benzi, R., Succi, S. & Vergassola, M. The lattice Boltzmann equation: theory and application. *Phys. Rep.* **222**, 145–197 (1992).
25. Mendoza, M., Boghosian, B. M., Herrmann, H. J. & Succi, S. Fast lattice Boltzmann solver for relativistic hydrodynamics. *Phys. Rev. Lett.* **105**, 014502 (2010).
26. Mendoza, M., Boghosian, B. M., Herrmann, H. J. & Succi, S. Derivation of the lattice Boltzmann model for relativistic hydrodynamics. *Phys. Rev. D* **82**, 105008 (2010).
27. Gabbana, A., Simeoni, D., Succi, S. & Tripiccione, R. Relativistic lattice Boltzmann methods: theory and applications. *Phys. Rep.* **863**, 1–63 (2020).
28. Romatschke, P., Mendoza, M. & Succi, S. A fully relativistic lattice Boltzmann algorithm. *Phys. Rev. C* **84**, 034903 (2011).
29. Romatschke, P. Relativistic (lattice) Boltzmann equation with nonideal equation of state. *Phys. Rev. D* **85**, 065012 (2012).
30. Gabbana, A., Mendoza, M., Succi, S. & Tripiccione, R. Numerical evidence of electron hydrodynamic whirlpools in graphene samples. *Comput. Fluids* **172**, 644–650 (2018).
31. Weih, L. R. et al. Beyond moments: relativistic lattice Boltzmann methods for radiative transport in computational astrophysics. *Mon. Notices R. Astron. Soc.* **498**, 3374–3394 (2020).
32. Ambruş, V. E. & Blaga, R. High-order quadrature-based lattice Boltzmann models for the flow of ultrarelativistic rarefied gases. *Phys. Rev. C* **98**, 035201 (2018).
33. Coelho, R. C. V., Mendoza, M., Doria, M. M. & Herrmann, H. J. Fully dissipative relativistic lattice Boltzmann method in two dimensions. *Comput. Fluids* **172**, 318–331 (2018).
34. Bazzanini, L., Gabbana, A., Simeoni, D., Succi, S. & Tripiccione, R. A lattice Boltzmann method for relativistic rarefied flows in (2+1) dimensions. *J. Comput. Sci.* **51**, 101320 (2021).
35. Ahrens, C. & Beylkin, G. Rotationally invariant quadratures for the sphere. *Proc. R. Soc. A* **465**, 3103–3125 (2009).
36. Gabbana, A. et al. Dissipative hydrodynamics of relativistic shock waves in a quark gluon plasma: comparing and benchmarking alternate numerical methods. *Phys. Rev. C* **101**, 064904 (2020).
37. Cercignani, C. & Kremer, G. M. *The Relativistic Boltzmann Equation: Theory and Applications* (Birkhäuser Basel, 2002).
38. Ambruş, V. E. & Guga-Roşian, C. Lattice Boltzmann study of the one-dimensional boost-invariant expansion with anisotropic initial conditions. *AIP Conference Proc.* **2071**, 020014 (2019).
39. Bjorken, J. D. Highly relativistic nucleus–nucleus collisions: the central rapidity region. *Phys. Rev. D* **27**, 140–151 (1983).
40. Heller, M. P. & Spalinski, M. Hydrodynamics beyond the gradient expansion: resurgence and resummation. *Phys. Rev. Lett.* **115**, 072501 (2015).
41. Soloviev, A. Hydrodynamic attractors in heavy ion collisions: a review. *Eur. Phys. J. C* **82**, 319 (2022).
42. Kurkela, A., Wiedemann, U. A. & Wu, B. Flow in AA and pA as an interplay of fluid-like and non-fluid like excitations. *Eur. Phys. J. C* **79**, 965 (2019).
43. Giacalone, G., Mazeliauskas, A. & Schlichting, S. Hydrodynamic attractors, initial state energy and particle production in relativistic nuclear collisions. *Phys. Rev. Lett.* **123**, 262301 (2019).
44. Ambruş, V. E., Schlichting, S. & Werthmann, C. Development of transverse flow at small and large opacities in conformal kinetic theory. *Phys. Rev. D* **105**, 014031 (2022).

45. Strickland, M. & Tantary, U. Exact solution for the non-equilibrium attractor in number-conserving relaxation time approximation. *JHEP* **10**, 069 (2019).

46. Kamata, S., Martinez, M., Plaschke, P., Ochsenfeld, S. & Schlichting, S. Hydrodynamization and nonequilibrium Green's functions in kinetic theory. *Phys. Rev. D* **102**, 056003 (2020).

47. Blaizot, J. P. & Yan, L. Attractor and fixed points in Bjorken flows. *Phys. Rev. C* **104**, 055201 (2021).

48. Ambruş, V. E., Busuioc, S., Fotakis, J. A., Gallmeister, K. & Greiner, C. Bjorken flow attractors with transverse dynamics. *Phys. Rev. D* **104**, 094022 (2021).

49. Romatschke, P. Relativistic fluid dynamics far from local equilibrium. *Phys. Rev. Lett.* **120**, 012301 (2018).

50. Adamczyk, L., STAR Collaboration. Global Λ hyperon polarization in nuclear collisions: evidence for the most vortical fluid. *Nature* **548**, 62–65 (2017).

51. Adam, J., STAR Collaboration. Global polarization of Λ hyperons in Au + Au collisions at $\sqrt{s_{NN}}$= 200 GeV. Phys. Rev. C 98, 014910 (2018).

52. Fukushima, K., Kharzeev, D. E. & Warringa, H. J. The chiral magnetic effect. *Phys. Rev. D* **78**, 074033 (2008).

53. Kharzeev, D. E., Liao, J., Voloshin, S. A. & Wang, G. Chiral magnetic and vortical effects in high-energy nuclear collisions—a status report. *Prog. Part. Nucl. Phys.* **88**, 1–28 (2016).

54. Ambruş, V. E. & Chernodub, M. N. Hyperon-anti-hyperon polarization asymmetry in relativistic heavy-ion collisions as an interplay between chiral and helical vortical effects. *Eur. Phys. J. C* **82**, 61 (2022).

55. Ambruş, V. E. & Chernodub, M. N. Vortical effects in Dirac fluids with vector, chiral and helical charges. Preprint at https://arxiv.org/abs/1912.11034 (2019).

56. Becattini, F. et al. A study of vorticity formation in high energy nuclear collisions. *Eur. Phys. J. C* **75**, 406 (2015).

57. Becattini, F., Chandra, V., Del Zanna, L. & Grossi, E. Relativistic distribution function for particles with spin at local thermodynamical equilibrium. *Ann. Phys.* **338**, 32–49 (2013).

58. Karpenko, I. & Becattini, F. Study of Λ polarization in relativistic nuclear collisions at $\sqrt{s_{NN}}$ = 7.7-200 GeV. *Eur. Phys. J. C* **77**, 213 (2017).

59. Friman, B., Florkowski, W., Jaiswal, A., Ryblewski, R. & Speranza, E. Relativistic fluid dynamics of spin-polarized systems of particles. In *Proc. XIII Quark Confinement and the Hadron Spectrum – PoS(Confinement2018)* Vol. 336, 158 (PoS, 2019).

60. Gabbana, A., Simeoni, D., Succi, S. & Tripiccione, R. Probing bulk viscosity in relativistic flows. *Philos. Trans. R. Soc. A* **378**, 20190409 (2020).

61. Kovtun, P. K., Son, D. T. & Starinets, A. O. Viscosity in strongly interacting quantum field theories from black hole physics. *Phys. Rev. Lett.* **94**, 111601 (2005).

62. Zhang, Y. et al. Temperature-dependent shear viscosity in a multi-phase transport model for ultrarelativistic heavy-ion collisions at RHIC and LHC. *J. Phys. G* **46**, 055101 (2019).

63. Niemi, H., Denicol, G. S., Huovinen, P., Molnár, E. & Rischke, D. H. Influence of shear viscosity of quark–gluon plasma on elliptic flow in ultrarelativistic heavy-ion collisions. *Phys. Rev. Lett.* **106**, 212302 (2011).

64. Calore, E. et al. Massively parallel lattice–Boltzmann codes on large GPU clusters. *Parallel Comput.* **58**, 1–24 (2016).

65. Calore, E., Gabbana, A., Kraus, J., Schifano, S. F. & Tripiccione, R. Performance and portability of accelerated lattice Boltzmann applications with OpenACC. *Concurr. Comput.* **28**, 3485–3502 (2016).

66. Di Staso, G., Clercx, H. J. H., Succi, S. & Toschi, F. Lattice Boltzmann accelerated direct simulation Monte Carlo for dilute gas flow simulations. *Philos. Trans. R. Soc. A* **374**, 20160226 (2016).

67. Fries, R. J., Müller, B., Nonaka, C. & Bass, S. A. Hadronization in heavy-ion collisions: recombination and fragmentation of partons. *Phys. Rev. Lett.* **90**, 202303 (2003).

68. Molnár, D. & Voloshin, S. A. Elliptic flow at large transverse momenta from quark coalescence. *Phys. Rev. Lett.* **91**, 092301 (2003).

69. Greco, V., Ko, C. M. & Lévai, P. Parton coalescence and the antiproton/pion anomaly at RHIC. *Phys. Rev. Lett.* **90**, 202302 (2003).

70. Bouras, I. et al. Relativistic shock waves in viscous gluon matter. *Phys. Rev. Lett.* **103**, 032301 (2009).

71. Bonaccorso, F. et al. LBcuda: a high-performance CUDA port of lbsoft for simulation of colloidal systems, 2022. *Comput. Phys. Commun.* **277**, 108380 (2022).

72. Succi, S. et al. Towards exascale lattice Boltzmann computing. *Comput. Fluids* **181**, 107–115 (2019).

73. Romatschke, P. Azimuthal anisotropies at high momentum from purely non-hydrodynamic transport. *Eur. Phys. J. C* **78**, 636 (2018).

74. Adamczyk, L., STAR Collaboration. Energy dependence of moments of net-proton multiplicity distributions at RHIC. *Phys. Rev. Lett.* **112**, 032302 (2014).

75. Habich, M. & Romatschke, P. Onset of cavitation in the quark–gluon plasma. *JHEP* **12**, 054 (2014).

76. Nahrgang, M., Bluhm, M., Schaefer, T., Thomas, B. & Steffen, A. Diffusive dynamics of critical fluctuations near the QCD critical point. *Phys. Rev. D* **99**, 116015 (2019).

77. Denicol, G. S., Molnár, E., Niemi, H. & Rischke, D. H. Resistive dissipative magnetohydrodynamics from the Boltzmann–Vlasov equation. *Phys. Rev. D* **99**, 056017 (2019).

78. Bacchini, F. et al. Fully kinetic shearing-box simulations of magnetorotational turbulence in 2D and 3D. I. Pair plasmas. Preprint at https://arxiv.org/abs/2206.07061 (2022).

79. Parise, G. et al. Lattice Boltzmann simulations of plasma wakefield acceleration. *Phys. Plasmas* **29**, 043903 (2022).

80. Anderson, J. L. & Witting, H. R. Relativistic quantum transport coefficients. *Physica* **74**, 489–495 (1974).

81. Anderson, J. L. & Witting, H. R. A relativistic relaxation-time model for the Boltzmann equation. *Physica* **74**, 466–488 (1974).

82. Landau, L. D. & Lifshitz, E. M. *Fluid Mechanics* (Elsevier, 1987).

83. Abramowitz, M., Stegun, I. A. & Miller, D. Handbook of mathematical functions with formulas, graphs and mathematical tables (National Bureau of Standards Applied Mathematics Series no. 55). *J. Appl. Mech.* **32**, 239 (1965).

84. Delsarte, P., Goethals, J. M. & Seidel, J. J. Spherical codes and designs. *Geom. Dedic.* **6**, 363–388 (1977).

85. Womersley, R. S. *Efficient Spherical Designs with Good Geometric Properties* (Springer, 2018).

86. Thompson, K. W. The special relativistic shock tube. *J. Fluid Mech.* **171**, 365–375 (1986).

87. Israel, W. Nonstationary irreversible thermodynamics: a causal relativistic theory. *Ann. Phys.* **100**, 310–331 (1976).

88. Israel, W. & Stewart, J. M. Thermodynamics of nonstationary and transient effects in a relativistic gas. *Phys. Lett. A* **58**, 213–215 (1976).

89. Jaiswal, A. Relativistic dissipative hydrodynamics from kinetic theory with relaxation time approximation. *Phys. Rev. C* **87**, 051901 (2013).

90. Romatschke, P. & Strickland, M. Collective modes of an anisotropic quark gluon plasma. *Phys. Rev. D* **68**, 036004 (2003).

91. Florkowski, W., Ryblewski, R. & Strickland, M. Testing viscous and anisotropic hydrodynamics in an exactly solvable case. *Phys. Rev. C* **88**, 024903 (2013).

92. Gabbana, A. & Ambruş, V. E. *Relativistic Lattice Boltzmann Method* (Code Ocean, 2022); https://doi.org/10.24433/CO.5625382.v2

Acknowledgements

Author contributions

A.G. R.T and S.S. conceived the research, L.B., A.G. and D.S. performed the numerical work related to the Riemann problem and the anisotropic flow, whereas V.E.A. performed the numerical work for the Bjorken flow. All authors contributed to the discussion of the results, the editing and revision of the paper.

Competing interests

The authors declare no competing interests.

Additional information

Supplementary information The online version contains supplementary material available at https://doi.org/10.1038/s43588-022-00333-x.

Correspondence and requests for materials should be addressed to D. Simeoni.

Peer review information *Nature Computational Science* thanks Paul Romatschke and the other, anonymous, reviewer(s) for their contribution to the peer review of this work. Handling editor: Jie Pan, in collaboration with the *Nature Computational Science* team. Peer reviewer reports are available.

Reprints and permissions information is available at www.nature.com/reprints.